Materials Today Bio 31 (2025) 101602

Contents lists available at ScienceDirect

Materials Today Bio

journal homepage: www.journals.elsevier.com/materials-today-bio

In situ tailored confining microenvironment for lung cancer spheroids

Yixiao Dong [a,f,*,1], Shuyi Qian [a,d,1], Xuechun Wang [a,d], Wang Zhang [a,d], Weisheng Lu [b], Ju Qu [a,d], Meihua Cui [a], Linzhi Chen [a,d], Yingshuai Zhao [e], Yuehua Gao [a,d], Monica Giomo [c], Anna Urciuolo [c,h], Jian Feng [g], Yijun Zheng [e], Biao Jiang [a,e], Ruling Shen [b,**], Xianmin Zhu [a,f], Nicola Elvassore [a,c,***]

[a] *Shanghai Clinical Research and Trial Center, Shanghai Institute for Advanced Immunochemical Studies (SIAIS), ShanghaiTech University, Shanghai, 201210, China*
[b] *Shanghai Laboratory Animal Research Center, Shanghai, 201203, China*
[c] *Department of Industrial Engineering, University of Padova, Padova, 35131, Italy*
[d] *School of Life Science and Technology, ShanghaiTech University, Shanghai, 201210, China*
[e] *School of Physical Science and Technology, ShanghaiTech University, Shanghai, 201210, China*
[f] *Shanghai Academy of Sciences & Technology Institute of Model Animals Transformation, Shanghai, 201203, China*
[g] *Department of Thoracic Surgery, Shanghai Chest Hospital, Shanghai Jiaotong University, Shanghai, 200030, China*
[h] *Department of Molecular Medicine, University of Padova, Padova, 35127, Italy*

ARTICLE INFO

Keywords:
Cancer
Bioprinting
Confinement
ECM mechanics
Two-photon lithography

ABSTRACT

The mechanical properties and physical confinement of the extracellular matrix (ECM) are crucial roles in regulating tumor growth and progression. Extensive efforts have been dedicated to replicating the physical characteristics of tumor tissue by developing two-dimensional (2D) and three-dimensional (3D) *in vitro* models. However, it remains a significant challenge to modulate the local microenvironment around the specific cells according to the culture progress. In this study, we develop a 3D culture platform for multicellular lung cancer spheroids using a gelatin-based hydrogel with adjustable density and stiffness. Then, by utilizing a two-photon mediated bioprinting technique, we construct 3D confining microstructures with micrometer accuracy to enclose the selected spheroids within the hydrogel matrix. Diverse transcriptional profilings of cells are observed in response to the increased ECM density and stiffness compared to the additional confining stress. In addition, changed confining stress can regulate the tumor cells with contrary impacts on the cell cycle-related pathways. Our model not only allows for modifications to the mechanical microenvironment of the overall matrix but also facilitates localized adjustments throughout the culture evolution. This approach serves as a valuable tool for investigating tumor progression and understanding cell-ECM interactions.

1. Introduction

Solid tumors are often recognized as complex desmoplastic tissues that are composed of heterogeneous cell populations, signaling molecules, and extracellular matrix (ECM) components. It has been widely documented that disrupted ECM mechanics in the tumor microenvironment (TME) plays a key role in promoting tumor progression [1]. For example, denser and stiffer tumor ECM is associated with enhanced cancer cell proliferation, metastasis, and drug resistance in multiple cancer types [2–5]. Recent studies emphasized that the cell-matrix interaction and confining stress can also impact the metabolism and metastatic cancer cell behaviors [6,7]. However, due to the complicated and dynamic features of TME, our understanding of how the physical and mechanical stimulation activates tumorigenic signaling pathways remains to be clarified.

During the last several decades, substantial efforts have been made to develop *in vitro* models to represent the ECM stiffness and microstructural features of tumor tissues. Early studies mostly focused on the two-

* Corresponding author. Shanghai Clinical Research and Trial Center, Shanghai Institute for Advanced Immunochemical Studies (SIAIS), ShanghaiTech University, Shanghai, 201210, China.
** Corresponding author.
*** Corresponding author. Department of Industrial Engineering, University of Padova, Padova 35131, Italy.
E-mail addresses: dongyx@shanghaitech.edu.cn (Y. Dong), shenruling@slarc.org.cn (R. Shen), nicola.elvassore@unipd.it (N. Elvassore).
[1] These authors contributed equally to this work.

https://doi.org/10.1016/j.mtbio.2025.101602
Received 27 November 2024; Received in revised form 15 February 2025; Accepted 19 February 2025
Available online 19 February 2025

dimensional (2D) cell cultures on the top of elastic substrates with different stiffnesses [8]. These models are easy to operate and convenient for screening mechanotransduction factors along with the gradient or high-throughput settings [9,10]. Growing evidence has indicated that cells can sense and respond to mechanical stimulations differently in 2D and three-dimensional (3D) contexts [11,12]. Therefore, many 3D culture platforms have been developed from natural and synthetic biomaterials, in which hydrogels are the most widely adopted due to their close biophysical characteristics to the natural tissue [13]. The hydrogel stiffness is commonly controlled by altering the material components and cross-linking density, but it is challenging to precisely modulate the local ECM microstructures around certain cells and to observe specific cell-ECM communications in a bulk hydrogel system. In addition, cancer cells may adopt a collective migration mode while retaining intercellular junctions in a 3D environment [14]. Thus, recent efforts have been made to develop 3D organ-like cultures such as multicellular spheroids and organoids within physiologically relevant circumstances [15,16].

On the other hand, Micro Electro Mechanical Systems (MEMS) based techniques provide a powerful tool for studying the cellular behaviors in a microscale confining geometry by constructing polydimethylsiloxane (PDMS) or hydrogel-based micro-patterns [17,18]. These devices are mostly used in 2D or 2.5D models and rely on pre-manufactured casting molds, in which the microstructural settings are not easy to revise in a timely manner. In contrast, 3D bioprinting allows more flexible building of complex constructs. Nonetheless, conventional 3D bioprinting platforms can be restricted by their printing resolution (typically around 100 μm) and capability of modulation in a pre-existing matrix [19]. In this context, Taale et al. recently demonstrated an interesting model for breast cancer spheroids migrating through a "dome-shaped" confinement created by two-photon lithography (TPL) [20]. Thanks to the highly confined focus of two-photon absorption, 3D microstructures with high spatial resolution were fabricated surround the cancer cell spheroids. Yet, the cancer spheroids were attached to a glass surface which did not recur the 3D migration scene. Previously, our group reported a unique bioprinting platform that relied on a multiphoton confocal microscope for *in situ* constructing 3D microstructures within cell-loaded Matrigel® or animal organs [21]. However, the strength of Matrigel® was too weak to simulate the tumor tissue and not easy to modulate for the mechanobiological studies.

In this study, we tended to develop a tailorable biomimetic model for cancer spheroids with controlled ECM density, stiffness, and *in situ* modification capability (Fig. 1). First, we established a bulk hydrogel for encapsulating lung cancer spheroids, from a hyperbranched polyethylene glycol (PEG)-based polymer cross-linking with thiolated gelatin [22]. The hydrogel stiffness can be controlled by altering the material concentration and cross-linking ratio [22,23]. Moreover, the hyperbranched polymer can be functionalized with a coumarin derivative serving as a photo-sensitive printable material. Then, we fabricated confining microstructures surrounding selected cancer spheroids *via* a "hydrogel-in-hydrogel" two-photon mediated bioprinting approach. Biochemical and transcriptional analyses of the cell spheroids from hydrogels revealed ECM density and changed local confining stress-regulated cancer cells through diverse mechanotransduction mechanisms. Overall, this tailorable hydrogel platform provides a comprehensive model for studying cell-ECM mechanotransduction in 3D.

2. Materials and methods

2.1. Synthesis of hyperbranched polyPEGDA

The hyperbranched polymer was synthesized by the Reversible Addition Fragmentation Chain Transfer (RAFT) polymerization approach as described previously [23]. Briefly, the monomer of poly (ethylene glycol) diacrylate (PEGDA, average M_n of 700 g mol^{-1}, Sigma-Aldrich) was dissolved in butanone at 0.4 mol L^{-1}. Then 2, 2′-Azobis(2-methylpropionitrile) (Sigma-Aldrich, 98 %) and R-2-cyanoprop-2-yl dithiobenzoate (Sigma-Aldrich, >97 %) were added into the mixture respectively as initiator and chain transfer agent (CTA), with the ratio of monomer:initiator:CTA = 25:0.5:1. After a half-hour of the argon purging, the reaction was performed in an oil bath at 65 °C. The polymerization was monitored by gel permeation chromatography (GPC) and terminated with desired molecular weight by exposure to air. The product was purified by precipitating in hexane/diethyl ether (1:2 v/v) solution, followed by dialysis against deionized water. The molecular weight (M_n) of the final product was around 16 kDa (with a Polydispersity Index of about 1.8). The pendant acrylate group on the polymer was approximately 50 mol percent calculated by ^{1}H NMR analysis.

2.2. Synthesis of hyperbranched PEG-CMMC

7-(Carboxymethoxy)-4-methylcoumarin (CMMC, Sigma-Aldrich, 97 %) was conjugated on the polyPEGDA in three steps. First, excess

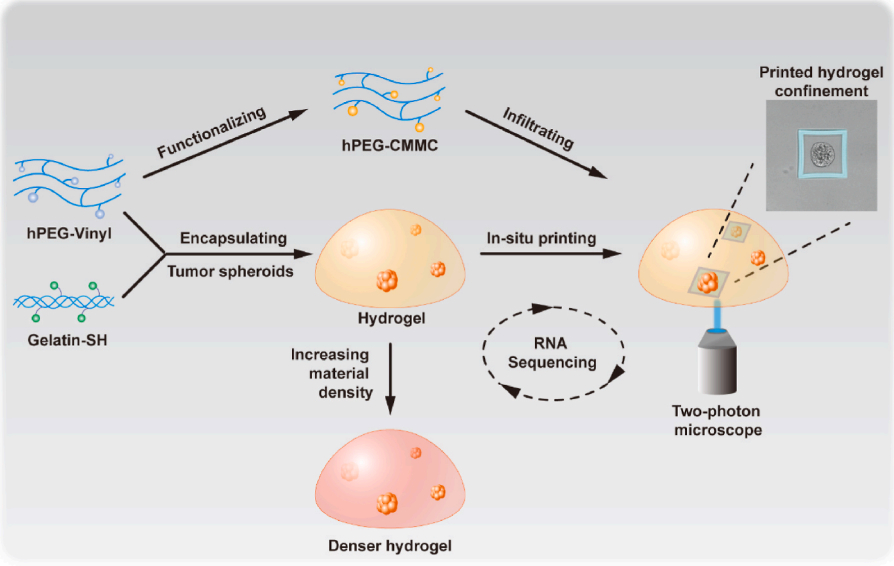

Fig. 1. Schematic of the establishment of mechanically tunable hydrogels and *in situ* construction of 3D confinements *via* two-photon mediated bioprinting.

cysteamine (Sigma-Aldrich, 95 %) was used to block all the acrylate groups on the hyperbranched ployPEGDA. The reaction was performed in deionized water for 2 h, and the product (polyPEG-NH_2) was dialyzed against deionized water followed by lyophilization. Meantime, CMMC (1 equiv.) was coupled with N-Hydroxysuccinimide (NHS, 2 equiv., Sigma-Aldrich, 97 %) and N,N′-Dicyclohexylcarbodiimide (DCC, 2 equiv., Sigma-Aldrich, 99 %) in anhydrous Dimethyl sulfoxide. The reaction was stirred at ambient temperature overnight in the dark, and the product was precipitated in excess diethyl ether followed by air drying. Then, the CMMC-NHS (2 equiv.) was conjugated to the amide groups on the hyperbranched polyPEG-NH_2 (1 equiv.) in anhydrous DMSO with triethylamine (TEA, 1 equiv., Sigma-Aldrich, 99.5 %). The reaction was stirred overnight in the dark followed by precipitation in excess diethyl ether. The final products were dialyzed for two days against 10 % (v/v) DMSO in deionized water and one day against deionized water, followed by lyophilization. The molecular structure of polyPEG-CMMC was assessed by ^{1}H NMR and the characterized absorption of CMMC around 320 nm was detected by UV–Vis spectrophotometer.

2.3. Hydrogel fabrication and rheological assessment

Thiolated gelatin was synthesized as previously reported [24]. Briefly, 2 g of gelatin (Sigma-Aldrich) was dissolved in 200 mL dH_2O and 2 g of 3,3′-dithiobis(propionic hydrazide) (DTP, J&K Scientific, 98 %) was added while stirring. The pH of the mixture was adjusted to 4.75 by 1M HCl, followed by adding 1 g of N-(3-Dimethylaminopropyl)-N′-ethylcarbodiimide hydrochloride (EDC, Sigma-Aldrich, 98 %). The reaction was maintained at a pH of 4.75 for 2 h and terminated by neutralizing the pH using 1M NaOH. Then 10 g of Dithiothreitol (DTT, Sigma-Aldrich, 99 %) was added into the reaction mixture at a pH of 8.5 and stirred for 24 h. The pH was adjusted to 3.5 after the reaction and the product was dialyzed against 0.3 mM HCl (pH 3.5) containing 100 mM NaCl, followed by an HCl solution without salt, then lyophilized after neutralizing the pH to 7.4. The final product was measured by ^{1}H NMR. For the hydrogel fabrication, the polyPEGDA was dissolved in Dulbecco's phosphate buffered saline (DPBS, Gibco), gently mixed with thiolated gelatin that dissolved in degassed dH_2O at desired concentrations, and the gelation occurred within about 5 min at room temperature. For mechanical analysis, 50 μL of precursor solution was pipetted on a hydrophobic Teflon surface to form the hydrogels with standardized shape, and the fully cross-linked samples were swollen in DPBS overnight pretesting. The storage (G′) and loss (G″) modulus were measured under a constant strain of 0.05 and frequency ranging from 0.1 to 10 rad s^{-1} at 25 °C, using a Discovery HR-2 Rheometer (TA Instruments) with steel parallel-plate geometry.

2.4. Cell culture and spheroid formation

A549 (Human lung carcinoma, epithelial, ATCC) cells were cultured in Roswell Park Memorial Institute (RPMI) 1640 medium (Gibco) supplemented with 10 % (v/v) of fetal bovine serum (FBS, Gibco) and 1 × Penicillin-Streptomycin (P/S, Gibco). The cells maintained the expected morphology with no mycoplasma detected and cultured at 37 °C in a humidified atmosphere containing 5 % (v/v) CO_2. For the spheroid formation, cell suspension was mixed with polyPEGDA-gelatin hydrogel precursor solution or Matrigel® (Corning) at a final concentration of 0.2 million cells per mL. 25 μL of hydrogel mixture was quickly pipetted on a Teflon surface and incubated at 37 °C in a humidified environment for 15 min for full gelation, then transferred into the culture medium. For the two-step culture approach, cell spheroids were collected from the Matrigel® after 6 days using Cell Recover Solution (Corning) and re-embedded in polyPEGDA-gelatin hydrogels at a density of about 40 spheroids in 25 μL of hydrogel. The spheroids-embedded hydrogels gelled in a circular PDMS mold (with an inner diameter of 8 mm) attached to a glass bottom culture dish for culturing, printing, and imaging. All samples were incubated at 37 °C in a humidified atmosphere containing 5 % (v/v) CO_2 with medium change every other day. LIVE/DEAD (Molecular Probes), alamarBlue™ (Invitrogen), and PicoGreen™ (Quant-iT, Invitrogen) assays were used to determine the viability and proliferation of the embedded cells and spheroids with recommended approaches.

2.5. Two-photon mediated bioprinting

As described above, 25 μL of polyPEGDA$_{(3\ \%,\ w/v)}$-gelatin$_{(2\ \%,\ w/v)}$ (G2) hydrogel (about 500 μm in height) was prepared in a circular PDMS mold (with an inner diameter of 8 mm) attached to a glass bottom culture dish. 40 μL of polyPEG-CMMC (30 %, w/v in DPBS) was added on the top of the hydrogel and penetrated at 37 °C in a humidified environment for 2 h. Leica SP8 Multiphoton confocal microscope (Leica Microsystems) was used for two-photon mediated bioprinting. The printing structures were designed with the ROI modulus of the Leica SP8 microscope. The operation settings were performed as follows: immersion objective (HC FLUOTAR L 25 × /0.95 water), laser wavelength (700 nm), laser power (40 % of nominal maximum laser power for printing the high-confining microstructures and 30 % of nominal maximum laser power for the rest), scanning speed (700 Hz), frame accumulation (6 for printing the high-confining microstructures and 4 for the rest), pixel resolution (512 × 512), zoom factor (1.85 ×) and stack depth (1 μm). After the printing, the hydrogel was washed with DPBS followed by the culture medium several times to remove the non-crosslinked polymer. To measure the mechanical properties of the printed hydrogel microstructures, the atomic force analysis was performed. The samples were printed through a thin layer of G2 hydrogel from the top surface on a glass coverslip and soaked in DPBS to avoid drying out. All measurements were performed by Atomic Force Microscope (AFM, Bruker) using a silicon nitride probe (with the F cantilever and a triangular tip, MLCT-BIO, Bruker) as previously reported [21]. Young's modulus was calculated by using the Bruker NanoScope Analysis software (Bruker, Santa Barbara, CA).

2.6. Real-time quantitative PCR

The hydrogels loaded with A549 cell spheroids were mechanically disrupted in TRIzol® LS reagent (Life Technologies). Total RNA was harvested *via* the phase separation in chloroform followed by purification using an RNeasy micro kit (Quigen). The reverse transcription was performed to the extracted RNA using a SuperScript® First-Strand Synthesis kit (Invitrogen), and real-time qPCR was completed by TaqMan® Gene Expression Master Mix (Applied Biosystems, CA). RNA samples from A549 cells plated on a standard tissue culture dish were used as the parallel control for normalization. The levels of GAPDH gene expression were quantified in parallel as an internal control.

2.7. Immunofluorescence

The spheroid-embedded hydrogels were fixed with 2 % (w/v) of paraformaldehyde containing 0.3 % (v/v) of glutaraldehyde (Sigma-Aldrich) at 4 °C. The samples were incubated with the primary antibodies (1:200) against Ki67 (Abcam, ab15580) and N-cadherin (Abcam, ab18203) at 4 °C overnight, followed by staining with Alexa Fluor 594-conjugated secondary antibody (1:1000, Invitrogen). Alexa Fluor 488/549 phalloidin (Invitrogen) and Hoechst 33258 (Invitrogen) were used to stain the filamentous actin (F-actin) and cell nuclei. The quantification analysis of Ki67 fluorescence intensity was normalized by DAPI intensity to reduce the effects of size deviation of the spheroids.

2.8. RNA sequencing

For RNA sequencing, cell spheroids were isolated from the hydrogels and frozen in liquid nitrogen. RNA was extracted by using Quick-RNA™ Microprep Kit (Zymo research). SMARTER mRNA-Seq Library Prep Kit

was used for the library preparation, and then sequencing was carried out in the Illumina Novaseq 6000 instrument. The raw data was handled by Skewer v0.2.2 and data quality was checked by FastQC (v0.11.2). Clean reads were aligned to the Human genome hg38 using StringTie (v1.3.1c). Then, the aligned reads were converted to counts using htseq. For the transcriptomic data analysis, differential expression analysis was conducted using DESeq2 (v1.34.0) in R. DEGs were determined by the filter criteria of P value < 0.05 and absolute $\log_2$ fold change >1. Heatmaps were plotted using the pheatmap R package calculated from scaled (Z-scores), normalized read counts in different samples. GO and KEGG enrichment analysis of the identified DEGs were performed by clusterProfiler (v4.2.2) package in R [25]. A P value < 0.05 was set as a threshold for significantly enriched terms. For GSEA, genes were ranked by $\log_2$ fold change value from DESeq2 to generate a single rank-ordered list, and analysis was performed using the "GSEA" function in the clusterProfiler package against the "h.all.v2023.1.Hs.symbols.gmt" MSigDB hallmark signatures (https://www.gsea-msigdb.org/gsea/msigdb/collections.jsp#H).

2.9. PPI network and module analysis

The protein-protein interaction (PPI) network of selected DEGs was established in the STRING database (https://cn.string-db.org) [26], and a confidence score >0.4 was set as the cut-off value. Then, Cytoscape [27] (v.3.9.1) was used to visualize the PPI networks and screen hub genes. Specifically, the Molecular Complex Detection (MCODE) plugin in Cytoscape was used to identify the key clustered modules in the PPI network of upregulated DEGs in stiff or confined groups, with a degree cutoff of 2, a node score cutoff of 0.2, and a K-Core of 2 [28].

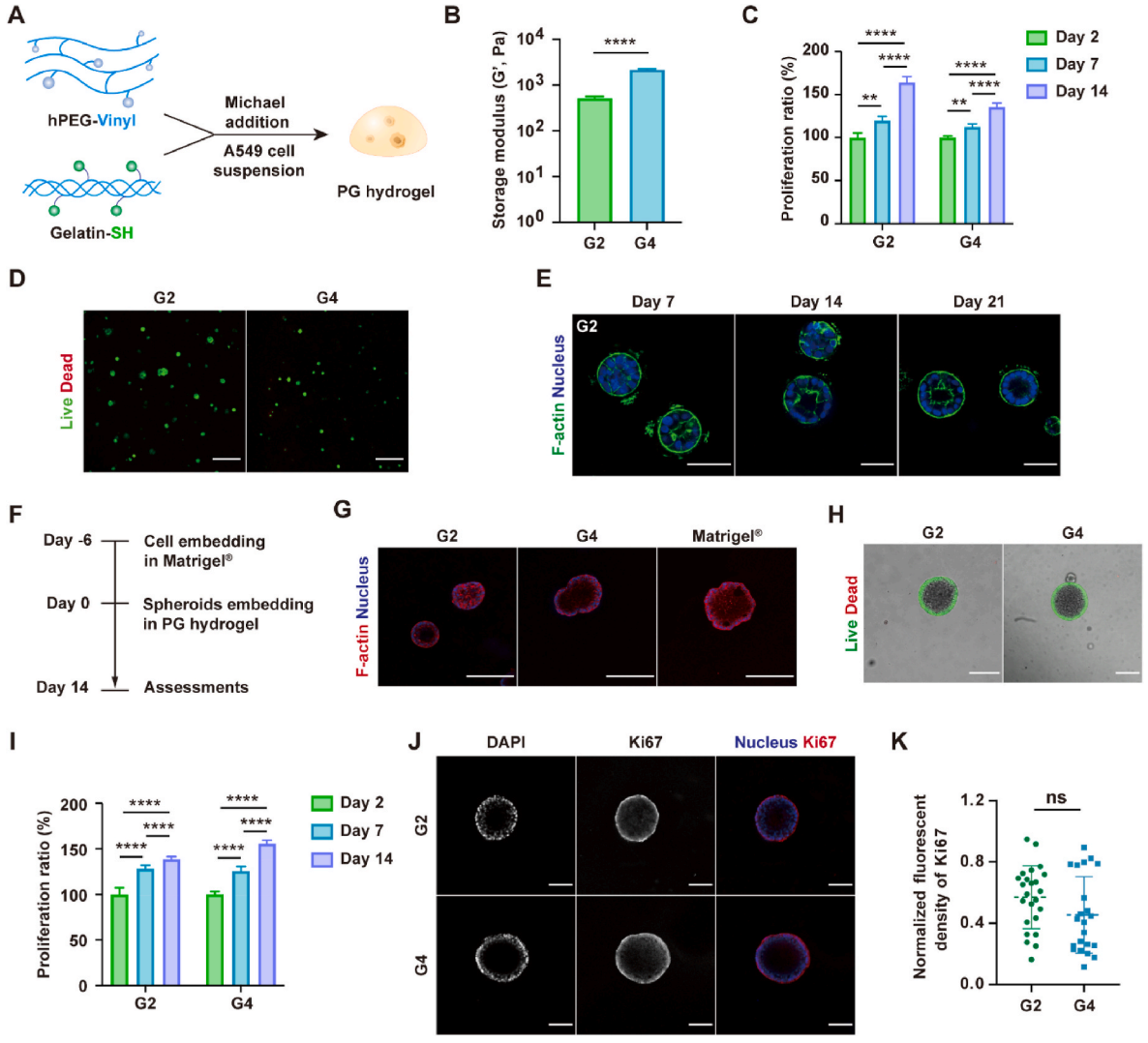

Fig. 2. Tunable polyPEGDA-Gelatin hydrogel for the 3D culture of A549 cancer cells. (A) Schematic of the fabrication of polyPEGDA-Gelatin (PG) hydrogels *via* Michael addition reaction. (B) The average storage modulus (G′) of P3G2 (G2) and P3G4 (G4) hydrogels. (C) The alamarBlue™ assay indicated the A549 cells proliferated in the PG hydrogels for up to 14 days. (D) LIVE/DEAD staining of embedded A549 cells in the hydrogels at day 14. Calcein AM (green) stain for live cells and ethidium homodimer-1 (red) for dead cells (scale bars: 200 μm). (E) Confocal images of A549 cell spheroids formed in G2 hydrogel, stained for filamentous actin (F-actin, green) and nucleus (blue) (scale bars: 50 μm). (F) Experimental schedule of 3D culturing A549 cell spheroids *via* a two-step approach. (G) Spheroid morphology at 7 days after re-embedded in G2, G4, and Matrigel®, stained for F-actin (red) and nucleus (blue) (scale bars: 200 μm). (H) LIVE/DEAD staining of cell spheroids in the PG hydrogels 14 days post re-embedding, merged with the bright field images (scale bars: 200 μm). (I) The alamarBlue™ assay of re-embedded cell spheroids in the PG hydrogels for up to 14 days. (J) Confocal images of Ki67 immunofluorescent staining (scale bars: 100 μm). (K) Quantification analysis of Ki67 fluorescence intensity normalized by DAPI intensity. (mean ± SD, n = 4, $^{****}P < 0.0001$, $^{**}P < 0.01$, ns, not statistically significant). (For interpretation of the references to colour in this figure legend, the reader is referred to the Web version of this article.)

2.10. Statistical analysis

GraphPad Prism 9 software (GraphPad Software, US) was used for the statistical analysis. All data are displayed as mean ± s.d. and a P value of <0.05 was considered significant, which was determined by unpaired two-tailed Student's t-tests, one-way ANOVA followed by Tukey's multiple comparison tests, or two-way ANOVA followed by Bonferroni's multiple comparison tests.

3. Results

3.1. Fabrication of tunable hydrogels for culturing lung cancer spheroids

To demonstrate our model for studying the mechanotransduction interplay between cancer cells and a controlled 3D microenvironment, we set up a hybrid hydrogel system to encapsulate lung cancer spheroids. First, a hyperbranched polymer of poly(ethylene glycol) diacrylate (polyPEGDA) was synthesized *via* the reversible addition-fragmentation chain transfer (RAFT) approach [23]. The molecular weight (M_n) of the polymer was around 16 kDa with pendent vinyl groups of about 50 mol %, measured by Gel Permeation Chromatography (GPC) and ^{1}H NMR analysis respectively (Fig. S1). To form the mechanically tunable hydrogels, the hyperbranched polyPEGDA was mixed with thiolated gelatin at different concentrations (referred to as PG hydrogels, Fig. 2A). The gelation occurred within 5 min at room temperature [22], and increased material density enhanced the mechanical strength of the hydrogels (Fig. 2B). For instance, the storage modulus (G') of hydrogels from 3 % (w/v) polyPEGDA with 2 % (w/v) thiolated gelatin (i.e. P3G2, G2) was 524.4 ± 43.6 Pa, whereas 2160.6 ± 115.1 Pa for the P3G4 (G4) hydrogel. Next, we encapsulated the A549 cell suspension into the PG hydrogels with varying material concentrations. The alamarBlue™ assay showed the cancer cells were able to proliferate inside the hydrogels (Fig. 2C), and the LIVE/DEAD assay confirmed that the hydrogel maintained cell viability over two weeks in both groups (Fig. 2D). Nonetheless, it seems the increased material density reduces the proliferation rate. In addition, the cancer cells formed a typical sphere structure only in the G2 hydrogel (Fig. 2E), but not in the stiffer hydrogels (data not shown). It was assumed that the restrained degradation in a denser matrix reduced cell assembling and spheroid formation. Thus, we tested the hydrogel degradation using collagenase. As expected, the hydrogel degradation was enzyme-dependent, and increased material density led to slower degradation (Fig. S2). These results suggested that the PG hydrogels can be used for the 3D culture of A549 cancer cells with tunable density and stiffness, but the spheroid formation was restricted in the denser matrix.

To avoid the above diversity, we optimized our approach by encapsulating cells in the Matrigel® at the first stage (Fig. 2F), and the multicellular spheroids were formed with the desired size (around 100 μm, Fig. S3) after 6 days. Then we digested the Matrigel® and re-embedded the spheroids into the G2 and G4 hydrogels. After culturing for another 7 days, similar 'acini' morphologies of cell spheroids were shown in the PG hydrogels and Matrigel® (Fig. 2G). The LIVE/DEAD assay indicated the cells remained alive in both G2 and G4 hydrogels after two weeks (Fig. 2H). Then we evaluated the cellular metabolic activity and proliferation by alamarBlue™ assay (Fig. 2I) and ki67 staining (Fig. 2J–K). A similar proliferating activity of embedded cell spheroids was shown within G2 and G4 hydrogels, which was further confirmed with the PicoGreen™ assay (Fig. S4) and size measurement (Fig. S5). These results suggested that the two-stage culture approach can effectively normalize the initial size and proliferation variances of cell spheroids cultured in hydrogels with different material densities. Overall, the G2 and G4 hydrogels support the growth and proliferation of embedded A549 cells, which showed potential as a 3D culture platform to identify cancer cell response to a tunable mechanical microenvironment.

3.2. Matrix density and stiffness reshape the transcriptional profile of A549 cell spheroids

To assess the regulation effects of hydrogel density and stiffness on the A549 cell spheroids at the transcriptional level, we manually picked up individual spheroids 14 days after incubating in the PG hydrogels and performed the RNA-seq analysis (Fig. 3A). Compared within the G2 hydrogel, cell spheroids in G4 hydrogel exhibited 2464 differentially expressed genes (DEGs) (Table S1). Gene Ontology (GO) analysis revealed that the upregulated DEGs were enriched in *cell-substrate junction*, *focal adhesion*, *lamellipodia*, and so forth (Fig. 3B), while the downregulated genes were mostly enriched in *catabolic process* (Table S1). Kyoto Encyclopedia of Genes and Genomes (KEGG) analysis showed that angiogenesis and metastasis-related pathways were upregulated including VEGF (vascular endothelial growth factor), HIF-1 (hypoxia-inducible factor-1), MAPK (mitogen-activated protein kinase), and FoxO (forkhead box O) signalings (Fig. 3C). We assumed that cancer spheroids in the denser hydrogel may generate a hypoxia microenvironment in the central that contributed to an angiogenesis effect through the HIF-1/VEGF signaling pathway [29–31]. Indeed, SEM images showed the G4 hydrogel exhibited an increased cross-linking density (Fig. S6), which led to a reduced permeation efficiency (Fig. S7). Gene Set Enrichment Analysis (GSEA) further identified the activation of the hypoxia pathway (Fig. 3D). Interestingly, we noticed that GSEA analysis also showed a decreased epithelial-mesenchymal transition (EMT) process for the A549 cell spheroids in the stiffer hydrogel (Fig. 3E). To confirm this result, we further tested the expression of key EMT marker genes by the qRT-PCR analysis and no significant difference was found between G2 and G4 hydrogel groups (Fig. 3F). Altogether, these results suggested that our tunable hydrogel model can effectively modulate the growth profile of collective cancer cells in a 3D microenvironment.

3.3. 3D bioprinting in hydrogels via two-photon microscopic platform

Next, we set up a two-photon mediated bioprinting platform to dynamically construct hydrogel microstructures enclosing the selected cancer cell spheroids in 3D circumstances. First, we conjugated the coumarin derivative of 7-(Carboxymethoxy)-4-methylcoumarin (CMMC) on the hyperbranched polyPEGDA (Fig. 4A and Fig. S8-S9). The micron-scale 3D hydrogel constructions can be printed with the functionalized hPEG-CMMC polymer using a multiphoton confocal microscope (Leica-TCS-SP8-MP). Dispense with any photoinitiators, CMMC groups on the polymer undergo intra/inter-molecular [2 + 2] cycloaddition under two-photon excitation at 700 nm [21]. With a custom-designed Region of Interest (ROI) combining the z-stack scanning process, the polymer molecule can cross-link at the laser focus region and form the desired 3D hydrogel pattern (Fig. 4B). Increased polymer concentration enhanced the photo-crosslinking intensity which was defined by the autofluorescence generated from the CMMC-cycloaddition (Fig. S10). Moreover, the unique hyperbranched polymeric structure and abundant pendent conjugating sites provide the polymer increased density of CMMC groups. Compared with our previously reported photosensitive materials of 4armPEG-CMMC and 8arm-PEG-CMMC, the hPEG-CMMC polymer showed higher characterized absorption of CMMC cycloaddition (Fig. S11) and more stable hydrogel architectures (Fig. S12).

Then, a "hydrogel-in-hydrogel" printing approach was applied to locally modify the microenvironment in the PG hydrogel (Fig. 4C). We first formed a G2 hydrogel with about 500 μm height on a glass bottom dish, and then dropped 30 % (w/v) of hPEG-CMMC polymer solution on the top of the hydrogel. According to the hydrogel density, polymer molecular weight, and hydrophilicity, the hPEG-CMMC polymer would diffuse into the PG hydrogel within a few minutes. A pilot test showed that stable hydrogel microstructure can be printed in the center of the PG hydrogel after 1h diffusion (Fig. 4D), and autofluorescence intensity

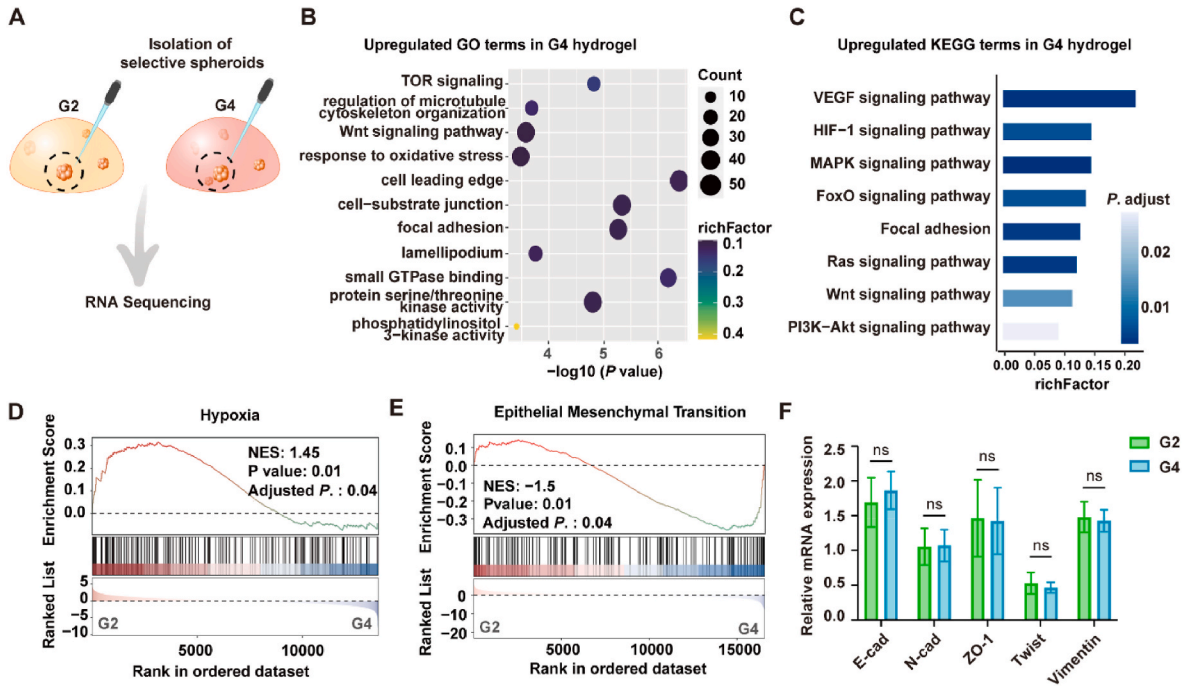

Fig. 3. Matrix stiffness affects the growth and transcriptional profile of A549 cell spheroids in PG hydrogels. (A) Schematic of spheroids extraction from G2 and G4 hydrogels for RNA sequencing. (B) GO enrichment analysis and (C) KEGG pathway analysis of the upregulated DEGs in the G4 hydrogels. A P value < 0.05 was defined as significantly enriched pathways. (D–E) GSEA plots show the enriched gene set of Hypoxia (D) and Epithelial-Mesenchymal Transition (EMT) (E) in the G4 hydrogels. (F) qRT-PCR analysis of key EMT-relevant gene expression in G2 and G4 hydrogels. RNA samples from A549 cells plated on a standard tissue culture dish were used as the parallel control for normalization, with GAPDH gene expression as an internal control (mean ± SD, n = 5, ns, not statistically significant).

of the printed microstructure reached a relative plateau after 2 h (Fig. 4E). Accordingly, we set a 2-h diffusion period in the following studies. To test the printing resolution of our platform, we printed a group of thin hydrogel strips designed with different widths and gaps. As a result, the thinnest hydrogel structure was obtained around 2 μm in width (Fig. 4F–G). It should be noted that these measurements display undisciplinable roughness limited by the imaging resolution. Besides, higher printing resolution can be achieved by changing the objective and optimizing the scanning setup (e.g. pixel resolution, scanning speed, etc.), whereas it was not the focus of this study. To evaluate the stability of the printed hydrogel microstructures in a culturing environment, we incubated the printed samples in PBS. It was shown that the thin hydrogel strips exhibited slight swelling in the first 2 days and then reached equilibrium (Fig. S13). Furthermore, we exhibited more complex hydrogel microstructures, such as curving logo, micron-pillar array, and crystal cell structures (Fig. 5A). We found that the swollen effect was not obvious when printing these larger-scale hydrogel structures. These results indicated that high-resolution hydrogel microstructures can be made with stable and relatively sharp constructions in the PG hydrogels.

3.4. *In situ bioprinting of confining microenvironment for tumor spheroids*

Next, to model a confining microenvironment for tumor cells, we designed a simple hydrogel parallelepiped (240 μm × 240 μm × 180 μm) to enclose the A549 cell spheroids, in which the ceiling and bottom side were left open to ensure the regular nutrition exchange (Fig. 5B). No obvious cell death was observed by LIVE/DEAD assay one day after we performed the *in situ* bioprinting approach (Fig. 5C), and the confined and unconfined cell spheroids showed similar morphology in the hydrogel after a few days of incubation (Fig. 5D). These results suggested our bioprinting process did not disturb the cell viability and growth. Then, we monitored the growing cell spheroids over two weeks to observe the interplay between cancer cells in the confining microenvironment. With the cell proliferation and spheroid expansion, enhanced confining stress would apply to the cancer cells due to the printed hydrogel structures are relatively not deformable. It was shown that once the cells occupied all the inner space, they pushed against the confining hydrogel and ultimately escaped from the top or bottom edges of the parallelepiped (Fig. 5E).

To estimate how the additional confining stress affects the tumor cell growth, we performed the transcriptome sequencing analysis for the selected confined and unconfined cell spheroids (Fig. 5F). The GO analysis indicated that A549 cell spheroids in the confining microenvironment exhibited enhanced expression in *cell-substrate adhesion*, *mitotic nuclear division*, and *nuclear division* (Fig. 5G and Table S2). The actin-binding and regulating genes (e.g. CDC42, NEDD9, RHOB, CTTN, ACTN1, and MYADM) were upregulated (Fig. 5H). KEGG analysis indicated an enhanced gene expression associated with the cell cycle and MAPK (mitogen-activated protein kinases) signaling pathway (Fig. S14A). GSEA analysis showed the enrichment in the EMT process in the confined cells (Fig. 5I and Fig. S14B).

3.5. *Matrix stiffness and confining stress impact A549 cell spheroids through diverse mechanotransduction pathways*

Overlapped alterations of the transcriptional pattern were observed for the cell spheroids in the denser hydrogel and the confining microenvironment (Fig. S15). We wondered whether they regulate the cancer cell progression through the unified signaling pathways. To answer this question, we analyzed the data from G2, G4, and confining groups together. Interestingly, the obvious distinctive clustering pattern was displayed between G4 and confining groups in the typical mechanotransduction pathways (Fig. 6A–B and Fig. S16-S17). To confirm our finding, we associated our data with known protein-protein interaction (PPI) databases and performed the PPI network analysis of the upregulated DEGs using the STRING database (Fig. 6C). As a result, two PPI networks were generated separately for the upregulated genes from G4 (including 1047 nodes and 5049 edges), and confining (including 248 nodes and 446 edges) groups, with a defined interaction score greater than 0.4. Then, key PPI module genes were extracted for further

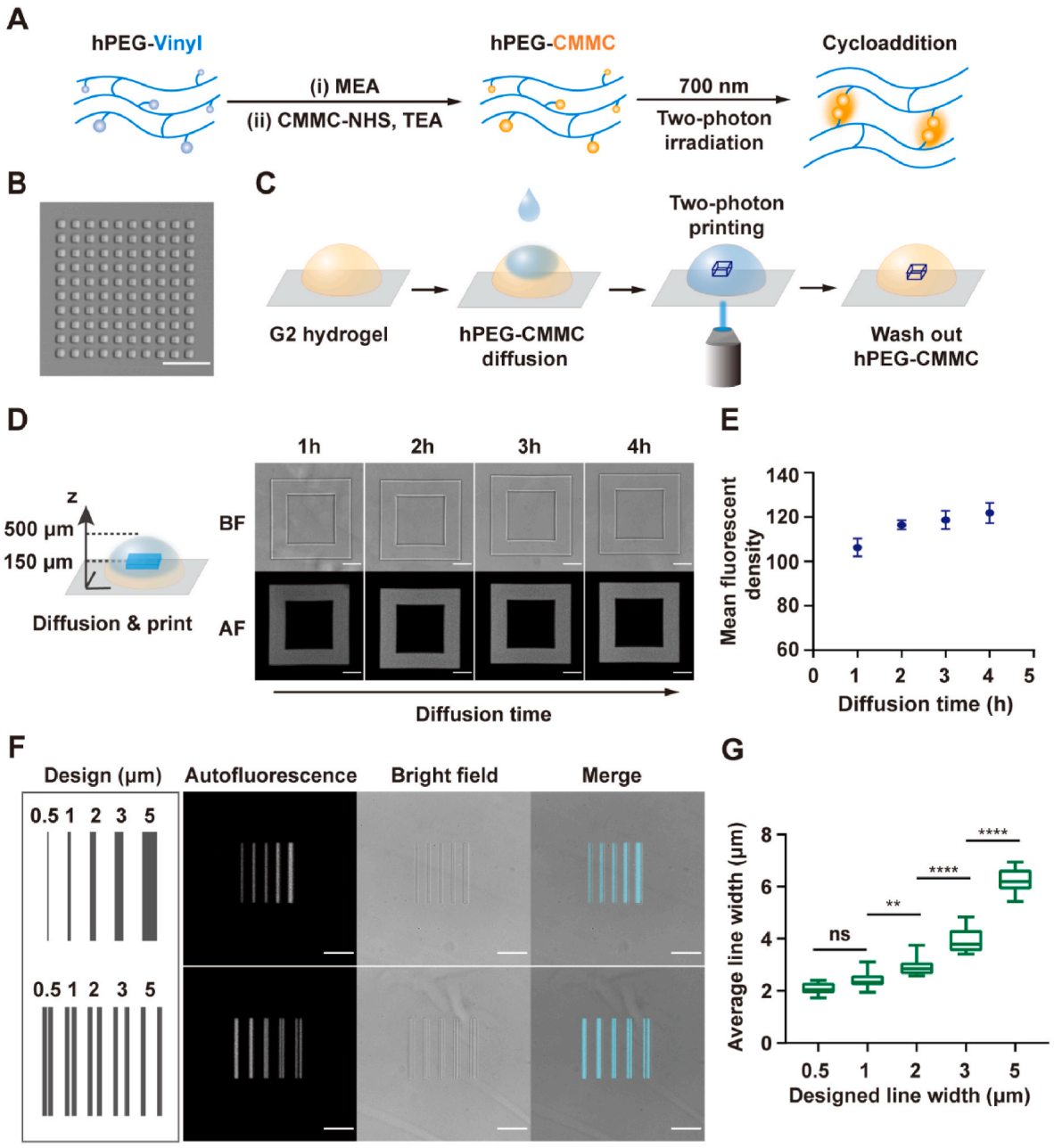

Fig. 4. ***In situ*** **"hydrogel-in-hydrogel" two-photon mediated printing platform.** (A) Schematic of conjugating photo-sensitive CMMC group on hyperbranched polyPEGDA (hPEG-CMMC), which can undergo intra/inter-molecular cycloaddion under two-photon excitation at 700 nm. (B) Bright field image of printed hydrogel micropattern (scale bar: 100 μm). (C) Schematic of *in situ* "hydrogel-in-hydrogel" printing strategy. (D) Diffusion and printing assessment in G2 hydrogel. Bright field (BF) and autofluorescence (AF) images indicated that stable microstructures can be achieved after 1 h (scale bars: 50 μm). (E) Quantification of autofluorescence density from printed hydrogel microstructures with increased diffusion time. (F) Assessment of printing resolution in G2 hydrogel (scale bars: 50 μm). (G) Measurement of line width from bright field images after printing. (mean ± SD, n = 6, $^{****}P < 0.0001$, $^{**}P < 0.01$, ns, not statistically significant).

enrichment analysis. In the G4 hydrogel, the hub genes showed enrichment in the FoxO signaling pathway, such as SIRT1, CDKN1B, AKT3, SMAD4, AKT2, MAPK8, CDKN1A, etc. (Fig. 6D–E and Table S3). Additionally, the Reactome analysis showed that the hub genes upregulated in the G4 hydrogel were significantly enriched in the *PI3K/AKT*, *AKT phosphorylates targets in the cytosol and nucleus*, and the *AKT-mediated inactivation of FOXO1A* (Table S4). In contrast, for the confining group, we found the hub genes were mainly enriched in the *cell cycle* and *cell division* process (Fig. 6F–G and Table S4). Specifically, we found that the cell division cycle (CDC)-associated genes (e.g. CDCA2, CDCA5, CDCA7, and CDCA8), kinesin family genes (e.g. KIF4 and KIF1C), and minichromosome maintenance complex component genes (e.g. MCM2 and MCM5) were significantly upregulated. These genes are involved in chromosome segregation and kinetochore-microtubule dynamics, regulating cell cycle and proliferation [32–34]. Collectively, these results implied that matrix stiffness and confining stress impact A549 cell spheroids through diverse mechanotransduction pathways according to our model.

3.6. *Enhanced confining stress impairs cell cycle progression in A549 cancer cell spheroids*

Next, we asked whether the locally confined cell spheroids would react differently to an enhanced confining stress in our model. To answer

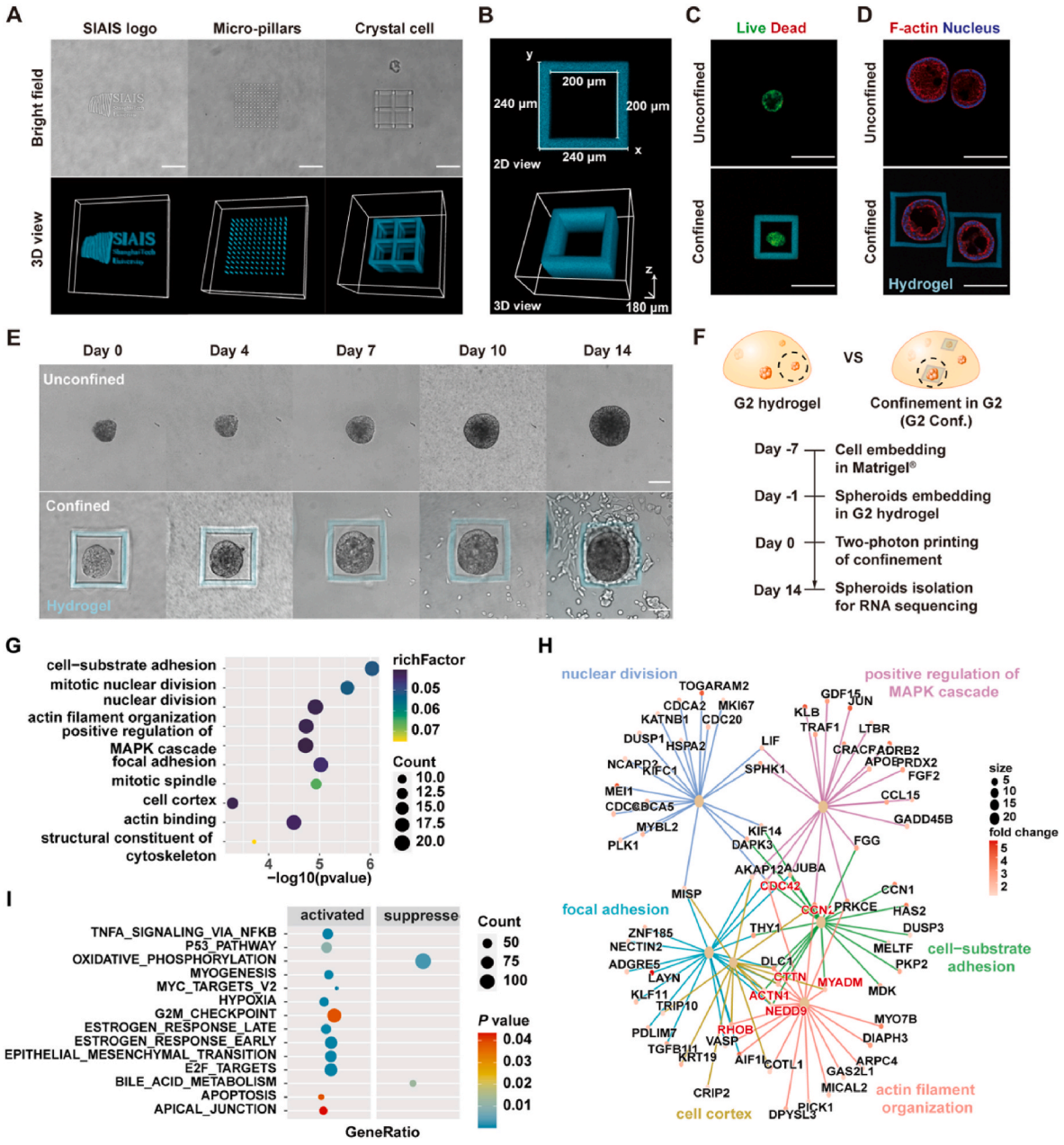

Fig. 5. *In situ* bioprinting **of confining microstructures for cancer cell spheroids**. (A) Bright field photos and 3D reconstruction of autofluorescence images of printed hydrogels with different geometries: institute logo (left), micropillar array (middle), and crystal cell structure (right) (scale bars: 100 μm). (B) Top-view and 3D reconstruction of printed confining parallelepiped. (C) LIVE/DEAD staining of A549 cell spheroids in G2 hydrogel one day post bioprinting (scale bars: 200 μm). (D) Spheroid morphology stained for F-actin (red), nucleus (blue), and autofluorescence of printed hydrogel confinements labeled as cyan (scale bars: 200 μm). (E) Representative images of unconfined and confined cell spheroids in G2 hydrogels for up to 14 days (scale bars: 100 μm). (F) Schematic of sample preparation for RNA sequencing. (G) GO enrichment analysis of the upregulated DEGs in the confining microenvironment. (H) Cnetplot representing the clustering of target genes based on gene ontology enrichment analysis. (I) GSEA using the Hallmarks gene sets shows significantly enriched pathways in the confining group. (For interpretation of the references to colour in this figure legend, the reader is referred to the Web version of this article.)

this question, we fabricated a narrower confining microenvironment by printing a smaller hydrogel parallelepiped (210 μm × 210 μm × 180 μm) with thicker walls (40 μm) (Fig. 7A). We also increased the laser power and the scanning accumulation to enhance the cross-linking density and mechanical strength of the printed hydrogel microstructure (Fig. 7B) [35,36]. Interestingly, we did not observe the obvious cell-escaping from these higher-confining hydrogel microstructures when the inner space was fully occupied (Fig. 7C). We extracted these cell spheroids (referred to as Conf. H) for transcriptome sequencing analysis and compared them with the above-described samples from G2 and confining (Conf.) groups. The hierarchical clustering results showed distinct total gene expression patterns for the three groups (Fig. 7D). The Venn diagram showed that 4943, 4940, and 396 DEGs were identified in 'Conf. H vs. Conf.', 'Conf. H vs. G2' and 'Conf. vs. G2" groups respectively (Fig. S18 and Table S5). Notably, we found the upregulated hub genes in the Conf. group were downregulated in the Conf. H group (Fig. 7E), while the downregulated genes in the Conf. H group showed enrichment in the *cell cycle phase transition*, *cell-substrate junction,* and *microtubule cytoskeleton organization* (Fig. 7F and Table S6). GSEA analysis further indicated the downregulation of the cell cycle-related genes within a higher confining microenvironment, such as *E2F targets*, *G2/M checkpoint*, and *Mitotic Spindle* (Fig. 7G–I). Taken together,

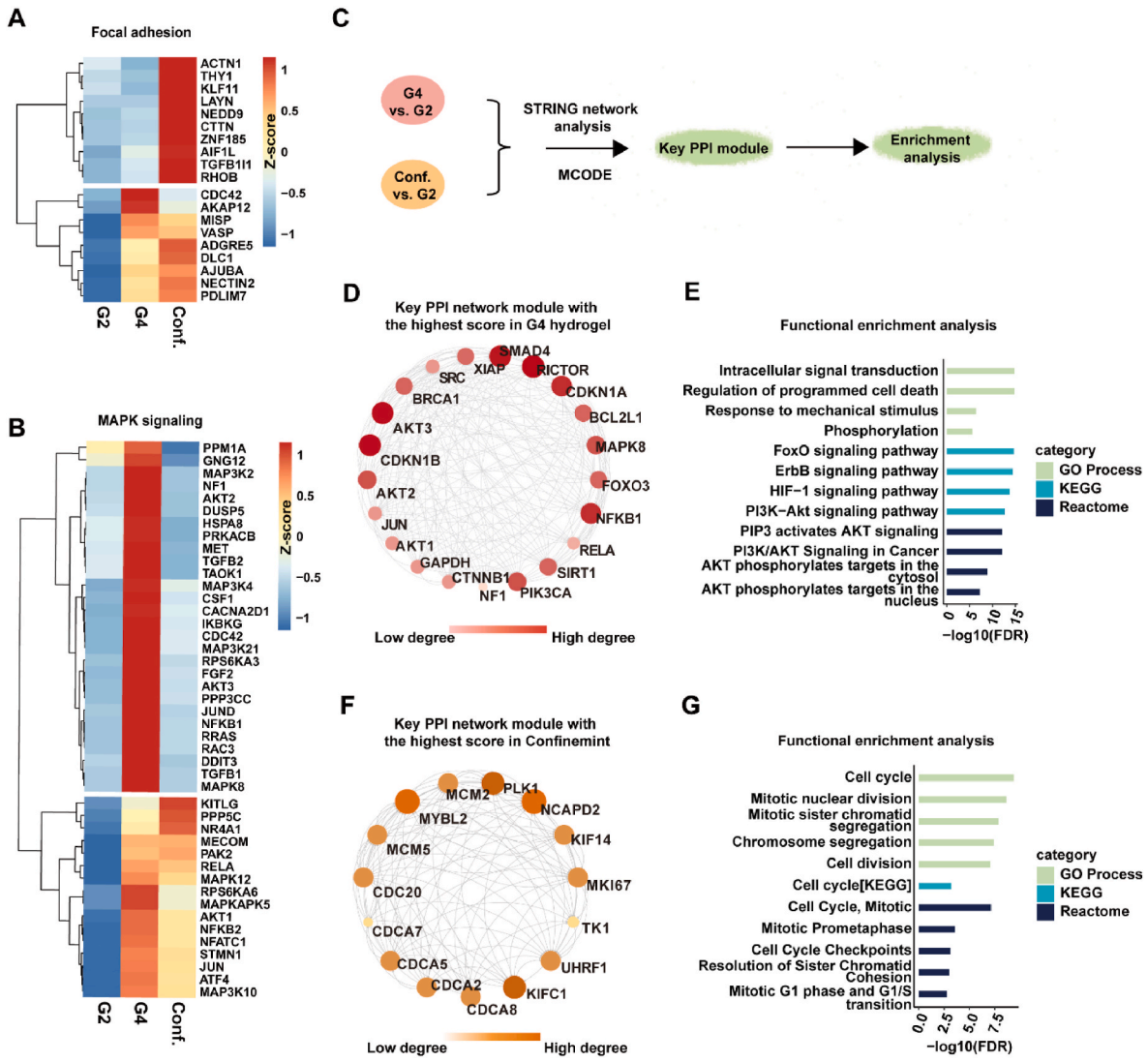

Fig. 6. Matrix stiffness and confinement induce different mechanotransduction pathways. (A–B) Heatmap normalized by z-score shows the DEGs involved in focal adhesion (A), and MAPK signaling pathway (B). The expression level was the mean of biological repeats. (C) Flow chart for identification of the hub genes by using String database and MCODE plug-in in Cytoscape software. (D) The key PPI module of upregulated DEGs in a stiff microenvironment with the highest score (score 19.1) extracted by the MCODE in Cytoscape. (E) Functional enrichment analysis for the key module genes from (D). (F) The key PPI module of upregulated DEGs in confinement with the highest score (score 14) was extracted by the MCODE in Cytoscape. (G) Functional enrichment analysis for the key module genes from (F). For (D) and (F), the darker and bigger the node is, the higher the interaction scores of the gene with other genes.

our results showed that unlike in the lower confining circumstance, cell cycle progression in A549 lung cancer spheroids was impaired by the higher confining stress.

4. Discussion

In this study, we have demonstrated a 3D *in vitro* model for studying cancer spheroids in a tailorable physical niche. Within a gelatin-based hydrogel, we observed the overall effects of altered material density and stiffness on the lung cancer spheroids in a 3D condition. By using a "hydrogel-in-hydrogel" *in situ* two-photon mediated bioprinting approach, we built micrometer-scale confining hydrogel structures around the live cell spheroids to timely modulate the local ECM microenvironment. Finally, we showed the local confining stress can regulate the tumor cells differently compared to the overall ECM density and stiffness in a bulk hydrogel.

The previous clinical data indicated that ECM density and tissue stiffness increased along with cancer progression, promoting immune cell infiltration, angiogenesis, and metastasis [37–39]. Here, we focus on lung cancer as one of the most commonly diagnosed cancer types, accounting for the highest mortality rates worldwide [40]. The stiffness of healthy lung parenchyma is around 0.2–5 kPa and can be significantly increased in lung tumors, as a result of the abnormal collagen cross-linking and ECM rearrangement [41]. Moreover, the increased ECM density and stiffness can trigger a feed-forward loop for activating cancer-associated fibroblasts (CAFs) producing more collagen and further stiffening the tumor ECM. By using a chemical cross-linked PG hydrogel system, we attempted to model the ECM microenvironment with altered material density and stiffness. However, when we directly encapsulated the cell suspension in the hydrogels, it was found the increased density restricted the cell-mediated degradation and impacted the spheroid formation (Fig. 2C–D). To solve this problem, we applied a two-step culture approach, in which more normalized cell spheroids were developed in the Matrigel® initially and then re-embedded into the G2 and G4 hydrogels with different densities and stiffness. In this way, we showed the similar morphology of cell spheroids cultured in both PG hydrogels (Fig. 2G). However, it should be noted that the various macromolecular compounds and growth factors in the Matrigel® may

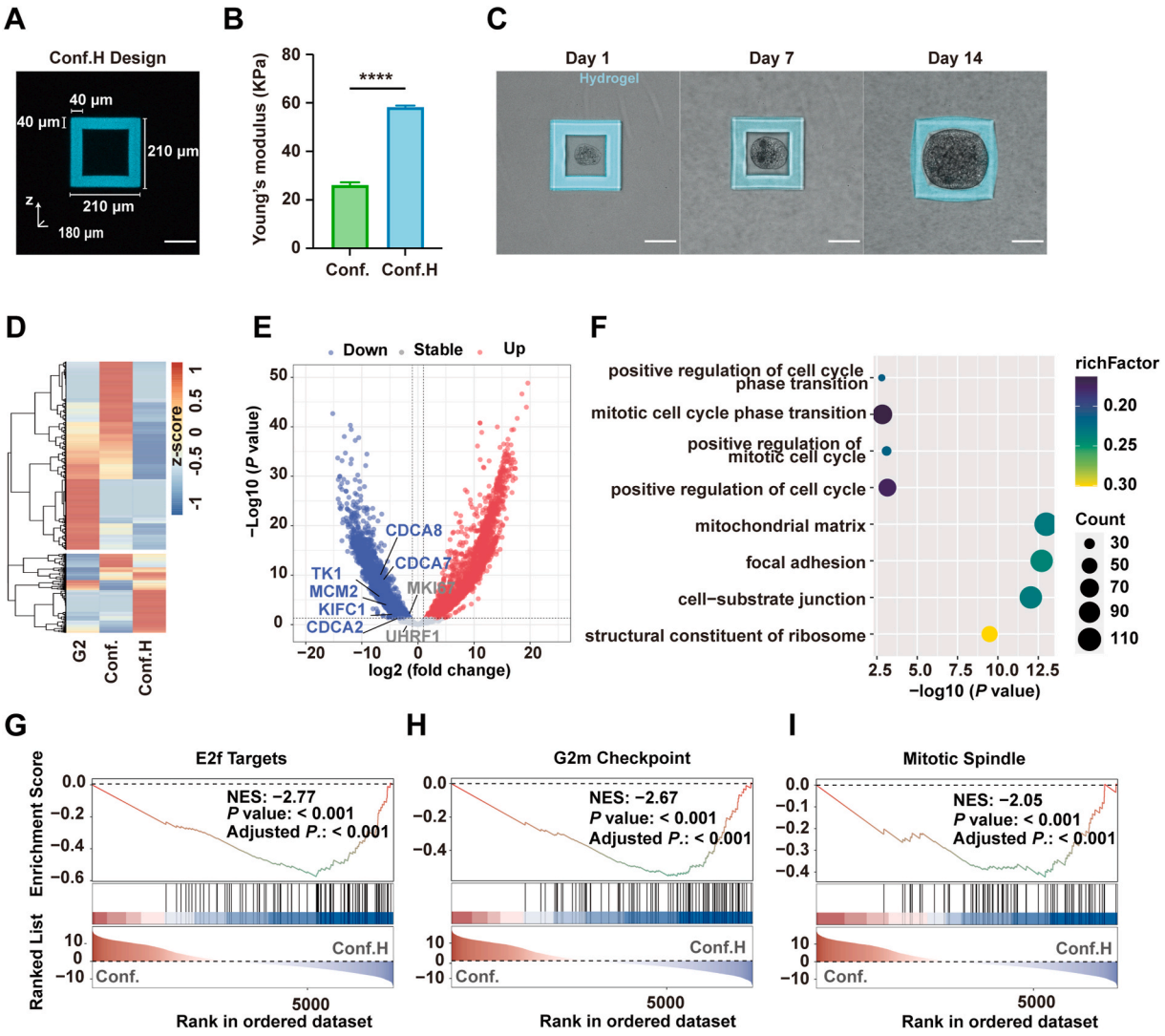

Fig. 7. Higher confinement impairs the cell cycle progress in A549 cell spheroids. (A) Top-view autofluorescence image of higher-confining (confining-H) hydrogel parallelepiped. (B) Young's modulus of the printed hydrogel confinements measured by atomic force microscopy (N = 3, mean ± s.d., ****p < 0.0001). (C) Representative images of A549 cell spheroids in higher confinement for up to 14 days. The autofluorescence of printed hydrogel confinements labeled as cyan (scale bars: 100 μm). (D) Heatmap normalized by z-score showing the gene expression of A549 cell spheroids in soft, confinement, and higher confinement groups. (E) Volcano plots of DEGs from higher confinement versus confinement. (F) GO enrichment analysis of the downregulated DEGs in higher confinement compared with the confinement group. (G–I) GSEA shows negative enrichment of E2F targets (G), G2M checkpoint (H), and Mitotic spindle (I) of A549 cell spheroids in higher confinement. (For interpretation of the references to colour in this figure legend, the reader is referred to the Web version of this article.)

cause unexpected biological activities for those tumor cells and further investigations would be necessary to answer this question.

Within our model, we indicated that the stiffer G4 hydrogel upregulated the gene expression mainly related to the *cell-substrate junction* and *focal adhesion* by the transcriptome sequencing analysis, which agreed with previous reports that showed stiffer substrates could enhance cell-ECM adhesions, stimulate microtubule formation, and promote cancer cell invasion [42–44]. Unexpectedly, we did not observe the typical EMT phenomenon in the G4 hydrogels (Fig. 3E–F). In principle, an increased ECM stiffness may regulate the integrin/FAK (focal adhesion kinase) signaling pathways in cancer cells and promote their proliferation and EMT, considered as a prerequisite for invasion and metastasis [45]. It was demonstrated that substrates-induced EMT can be associated with integrin-mediated TGF-β (transforming growth factor-β) activation dependent on Rho/ROCK (Rho-associated coiled-coil containing kinase) signaling [46] and the c-Myb-DDR2 (discoidin domain receptor 2) axis [47]. Yet, an argued study has shown that the substrate stiffness modulates the A549 cells as opposed to EMT signaling [48]. In addition, other microenvironment cues (e.g. soluble signals, local topography, and interstitial flow stress) can impact the cell behaviors responding to the altered ECM mechanics. For example, matrix topography can contribute to the stiffness-mediated EMT through the PI3K/Akt (Phosphoinositide 3-kinase/protein kinase B) signaling pathway in lung cancer cells [49]. On the other hand, the cells at the different regions (e.g. outward vs. inner) of the spheroid may receive distinct mechanical stimulation in a 3D condition, and our analysis methods cannot identify these spatial impacts. Applying more advanced spatial RNA-seq or ultra-high resolution live imaging techniques would be necessary for future investigations.

Apart from the bulk effect of matrix density and stiffness, local confining stress may also confer cancer cells a greater invading capability and chemotherapy resistance [50]. To build a confining microenvironment for the cancer cell spheroid, we applied an *in situ* two-photon mediated bioprinting within the soft PG (i.e. G2) hydrogels. Previously, we have reported this technical platform for printing the complex 3D hydrogel structures inside the tissue of live animals, using a commonly available multiphoton confocal microscope with the photo-sensitive coumarin-functionalized gelatin and starPEG polymers

[21]. We also showed the fabrication of the microstructures to temporally regulate the live organoids pre-cultured in the Matrigel® matrix [35]. However, it was found that printed micro-structures can be easily deformed along with the culture progressing. In this study, we first improved our photo-sensitive material by conjugating the active coumarin derivative (i.e. CMMC) on a hyperbranched polymer of polyPEGDA. With the unique hyperbranched polymeric structure and increased density of CMMC groups, the hPEG-CMMC polymer showed enhanced efficiency of CMMC cycloaddition and more stable hydrogel architectures after the printing (Figs. S11–12), which makes it possible for us to study the cell-EMC interplay in the printed confinements. Then, we built a parallelepiped hydrogel structure surrounding the cell spheroid as a simplified model of the confining microenvironment. With the spheroid expansion, the solid stress inside the printed hydrogel structure would be significantly increased, which is similar to the natural process of tumor invasion. As a limitation, the confined cells may confront different mechanical compressions at the square corner inside the hydrogel cube, whereas a spherical or arch shape would be more fitted to the cell spheroids. However, it has to be noted that building a spherical structure may take significant prolonged printing time. More importantly, the laser intensity will be different once it passes through a cell spheroid or cured hydrogel architecture for printing the top/bottom-side structures, which can cause uneven distribution of the hydrogel mechanical strength. To improve our platform, it would be helpful to upgrade the microscope software and operating algorithm for more intelligent control of the movement of the sample stage and laser compensation during the printing.

At the early stage of tumor progression, the uncontrolled growth of tumor cells and the excess of ECM produced by CAFs cause a crowded microenvironment with enhanced solid stress [51,52]. A former study showed that intratumoral compressive stress in a confined space enhances the EMT process in renal cell carcinoma [53]. Recent studies showed that confinement and compressive stress act as essential stimulators to induce CAF reorganization and form the contractile capsules which can actively compress the tumor growth [54,55]. In our study, with the spheroid expended and occupying the inner space of the printed structure, the outward cells on the spheroid tended to escape from the confinement with some leading cells disengaging from the spheroid at the edges. Comparably, a previous study indicated the compressive stress caused by the confined growth can stimulate the breast cancer cells forming a subpopulation of “leader cells” with enhanced cell-ECM adhesion and promoted invasiveness [56]. Our RNA-seq analysis confirmed the upregulation of the genes related to actin-binding (e.g. CDC42, NEDD9, RHOB, CTTN, ACTN1, and MYADM), which are known to regulate cancer cell migration and invasion *via* actin cytoskeleton organization [57–62].

According to our model, we found distinctive transcriptional patterns in the typical mechanotransduction (e.g. focal adhesion, MAPK, cell-substrate junction, and cell leading edge) pathways, regulated by the bulk hydrogel stiffness and the local confining stress (Fig. 6A–B and Fig. S16-S17). In contrast with the regulation impacts by the stiffer hydrogels, EMT-associated genes were upregulated by the confining microenvironment according to the GSEA analysis (Fig. 5I and Fig. S14B). In addition, the TGFB1I1 showed a fold increase in the confining group (Table S2), which can induce the formation of actin stress fiber to promote EMT and cancer cell migration [63,64]. The PPI network analysis further indicated that the FoxO associated with the PI3K/AKT signaling pathway is enriched by the regulation of the stiffer hydrogels (Fig. 6D–E). Consistently, previous studies have reported that FoxOs can be stimulated by mechanical signals [65,66], and are often regulated by the oncogenic PI3K/AKT pathway in cancers *via* AKT-mediated phosphorylation [67]. On the other hand, the printed confining structures upregulated the genes in the cell division cycle and proliferation (Fig. 6F–G). However, we noted that the contradictory results were reported previously based on the PDMS-based microdevices, in which the increased solid stress would impair the mitosis and cell cycle progression for both single and collective cancer cells [68,69]. More recently, the Chaudhuri group indicated breast cancer cell spheroids were mostly arrested in the G0/G1 phase in a slow-relaxing hydrogel (higher confinement), while the fast-relaxing hydrogels (lower confinement) promote cell cycle progression [70]. Therefore, we fabricated a stiffer confining hydrogel parallelepiped with a narrower inner space to amplify the compressive stress in our model. As a result, we found the opposite regulating effects to the relative genes between the “confining” and “higher confining” groups, where the cell cycle-related genes were downregulated within the higher confining microenvironment (Fig. 7G–I). It should be noted that the stiffness of the printed microstructures and the surrounding local mechanical microenvironment can be constantly changing along with the cell culture evolution, due to the ECM degradation and the contractile force by nearby embedded cells. In addition, we found the expression of the mechanotransduction factors might not be evenly distributed in the whole spheroid inside the confinement but was highly relative to the regional interaction between cell and printed structures (Fig. S19). Therefore, the conventional staining method and the bulk transcriptome analysis in this study cannot cover the whole story. Nonetheless, our tunable hydrogel and high-resolution 3D bioprinting platform combined with advanced methodologies such as spatial omics, local force measurement, and ultra-high resolution live imaging techniques would potentially benefit our understanding of 3D spheroid mechanobiology.

5. Conclusion

In this study, we have described the development of a tunable hydrogel-based 3D culture platform for lung cancer cell spheroids. We showed the controllable mechanical property of the bulk hydrogel system and enabled to flexibly fabricating of a confinement surrounding the selected cell spheroids by two-photon mediated high-resolution bioprinting. Through our platform, we demonstrated distinguishing mechanotransduction mechanisms affected by the overall ECM density and local confining stress. This platform can potentially improve the current 3D organ-like culture methods and provide a powerful tool for studying the cell-ECM interplay in a confining microenvironment.

CRediT authorship contribution statement

Yixiao Dong: Writing – review & editing, Writing – original draft, Supervision, Methodology, Funding acquisition, Data curation, Conceptualization. **Shuyi Qian:** Writing – original draft, Visualization, Methodology, Investigation, Data curation. **Xuechun Wang:** Methodology, Investigation, Data curation. **Wang Zhang:** Investigation, Data curation. **Weisheng Lu:** Data curation. **Ju Qu:** Methodology, Investigation. **Meihua Cui:** Data curation. **Linzhi Chen:** Data curation. **Yingshuai Zhao:** Methodology. **Yuehua Gao:** Data curation. **Monica Giomo:** Methodology, Funding acquisition, Data curation. **Anna Urciuolo:** Writing – review & editing, Methodology. **Jian Feng:** Resources. **Yijun Zheng:** Resources, Methodology. **Biao Jiang:** Resources. **Ruling Shen:** Resources, Writing – review & editing. **Xianmin Zhu:** Writing – review & editing, Funding acquisition. **Nicola Elvassore:** Writing – review & editing, Funding acquisition, Conceptualization.

Declaration of competing interest

The authors declare that they have no known competing financial interests or personal relationships that could have appeared to influence the work reported in this paper.

Acknowledgements

This work was supported by the National Key Research and Development Program of China (2023YFA1800403); Experimental Animal Research Fund, Science and Technology Commission of Shanghai

Municipality (21140901500 and 22140900100); and Prot. BIRD 229205 from DII-University of Padova. We are grateful for the technical support from the Discovery Technology Platform and Biomedical Big Data Platform of ShanghaiTech University, the Molecular Imaging System, and the Integrated Laser Microscopy System at the National Facility for Protein Science Shanghai (NFPS). We sincerely thank constructive discussion with Dr. Lichun Jiang and Prof. Jie Zheng.

Appendix A. Supplementary data

Supplementary data to this article can be found online at https://doi.org/10.1016/j.mtbio.2025.101602.

Data availability

Data will be made available on request.

References

[1] M.J. Bissell, W.C. Hines, Why don't we get more cancer? A proposed role of the microenvironment in restraining cancer progression, Nat. Med. 17 (3) (2011) 320–329.
[2] D. Pankova, Y.Y. Jiang, M. Chatzifrangkeskou, I. Vendrell, J. Buzzelli, A. Ryan, C. Brown, E. O'Neill, RASSF1A controls tissue stiffness and cancer stem-like cells in lung adenocarcinoma, EMBO J. 38 (13) (2019) e100532.
[3] O. Chaudhuri, S.T. Koshy, C.B. da Cunha, J.W. Shin, C.S. Verbeke, K.H. Allison, D. J. Mooney, Extracellular matrix stiffness and composition jointly regulate the induction of malignant phenotypes in mammary epithelium, Nat. Mater. 13 (10) (2014) 970–978.
[4] Y.A. Miroshnikova, J.K. Mouw, J.M. Barnes, M.W. Pickup, J.N. Lakins, Y. Kim, K. Lobo, A.I. Persson, G.F. Reis, T.R. McKnight, E.C. Holland, J.J. Phillips, V. M. Weaver, Tissue mechanics promote IDH1-dependent HIF1α-tenascin C feedback to regulate glioblastoma aggression, Nat. Cell Biol. 18 (12) (2016) 1336–1345.
[5] J. Schrader, T.T. Gordon-Walker, R.L. Aucott, M. van Deemter, A. Quaas, S. Walsh, D. Benten, S.J. Forbes, R.G. Wells, J.P. Iredale, Matrix stiffness modulates proliferation, chemotherapeutic response, and dormancy in hepatocellular carcinoma cells, Hepatology 53 (4) (2011) 1192–1205.
[6] O. Ilina, P.G. Gritsenko, S. Syga, J. Lippoldt, C.A.M. La Porta, O. Chepizhko, S. Grosser, M. Vullings, G.J. Bakker, J. Starruss, P. Bult, S. Zapperi, J.A. Käs, A. Deutsch, P. Friedl, Cell-cell adhesion and 3D matrix confinement determine jamming transitions in breast cancer invasion, Nat. Cell Biol. 22 (9) (2020) 1103–1115.
[7] M. Wang, B. Cheng, Y.W. Yang, H. Liu, G.Y. Huang, L.C. Han, F. Li, F. Xu, Microchannel stiffness and confinement jointly induce the mesenchymal-amoeboid transition of cancer cell migration, Nano Lett. 19 (9) (2019) 5949–5958.
[8] R.J. Pelham, Y.L. Wang, Cell locomotion and focal adhesions are regulated by substrate flexibility, P Natl Acad Sci USA 94 (25) (1997) 13661–13665.
[9] J.D. Mih, A.S. Sharif, F. Liu, A. Marinkovic, M.M. Symer, D.J. Tschumperlin, A multiwell platform for studying stiffness-dependent cell biology, PLoS One 6 (5) (2011) e19929.
[10] W.J. Hadden, J.L. Young, A.W. Holle, M.L. McFetridge, D.Y. Kim, P. Wijesinghe, H. Taylor-Weiner, J.H. Wen, A.R. Lee, K. Bieback, B.N. Vo, D.D. Sampson, B. F. Kennedy, J.P. Spatz, A.J. Engler, Y.S. Choi, Stem cell migration and mechanotransduction on linear stiffness gradient hydrogels, P Natl. Acad. Sci. USA 114 (22) (2017) 5647–5652.
[11] A. Saraswathibhatla, D. Indana, O. Chaudhuri, Cell-extracellular matrix mechanotransduction in 3D, Nat. Rev. Mol. Cell Biol. 24 (7) (2023) 495–516.
[12] S.R. Caliari, S.L. Vega, M. Kwon, E.M. Soulas, J.A. Burdick, Dimensionality and spreading influence MSC YAP/TAZ signaling in hydrogel environments, Biomaterials 103 (2016) 314–323.
[13] L. Gu, D.J. Mooney, Biomaterials and emerging anticancer therapeutics: engineering the microenvironment, Nat. Rev. Cancer 16 (1) (2016) 56–66.
[14] K. Wolf, Y.I. Wu, Y. Liu, J. Geiger, E. Tam, C. Overall, M.S. Stack, P. Friedl, Multi-step pericellular proteolysis controls the transition from individual to collective cancer cell invasion, Nat. Cell Biol. 9 (8) (2007) 893–904.
[15] S. Gunti, A.T.K. Hoke, K.P. Vu, N.R. London, Organoid and spheroid tumor models: techniques and applications, Cancers 13 (4) (2021) 874.
[16] D. Vahala, S.E. Amos, M. Sacchi, B.G. Soliman, M.S. Hepburn, A. Mowla, J. Li, J. H. Jeong, C. Astell, Y. Hwang, B.F. Kennedy, K.S. Lim, Y.S. Choi, 3D volumetric mechanosensation of MCF7 breast cancer spheroids in a linear stiffness gradient GelAGE, Adv. Healthcare Mater. 12 (31) (2023) e2301506.
[17] A. Pathak, S. Kumar, Independent regulation of tumor cell migration by matrix stiffness and confinement, P Natl. Acad. Sci. USA 109 (26) (2012) 10334–10339.
[18] F. Sala, C. Ficorella, R. Osellame, J.A. Käs, R.M. Vázquez, Microfluidic lab-on-a-chip for studies of cell migration under spatial confinement, Biosens. Bioelectron. 12 (8) (2022) 604.
[19] Y. Xiang, K. Miller, J. Guan, W. Kiratitanaporn, M. Tang, S.C. Chen, 3D bioprinting of complex tissues in vitro: state-of-the-art and future perspectives, Arch. Toxicol. 96 (3) (2022) 691–710.
[20] M. Taale, B. Schamberger, F. Taheri, Y. Antonelli, A. Leal-Egaña, C. Selhuber-Unkel, In situ fabrication of constraints for multicellular micro-spheroids using two-photon lithography, Adv. Funct. Mater. (2023) 2302356.
[21] A. Urciuolo, I. Poli, L. Brandolino, P. Raffa, V. Scattolini, C. Laterza, G.G. Giobbe, E. Zambaiti, G. Selmin, M. Magnussen, L. Brigo, P. De Coppi, S. Salmaso, M. Giomo, N. Elvassore, Intravital three-dimensional bioprinting, Nat. Biomed. Eng. 4 (9) (2020) 901–915.
[22] Y. Dong, A. Sigen, M. Rodrigues, X. Li, S.H. Kwon, N. Kosaric, S. Khong, Y. Gao, W. Wang, G.C. Gurtner, Injectable and tunable gelatin hydrogels enhance stem cell retention and improve cutaneous wound healing, Adv. Funct. Mater. 27 (24) (2017) 1606619.
[23] Y. Dong, Y. Qin, M. Dubaa, J. Killion, Y. Gao, T. Zhao, D. Zhou, D. Duscher, L. Geever, G.C. Gurtner, W. Wang, A rapid crosslinking injectable hydrogel for stem cell delivery, from multifunctional hyperbranched polymers via RAFT homopolymerization of PEGDA, Polym. Chem. 6 (34) (2015) 6182–6192.
[24] X.Z. Shu, Y.C. Liu, F. Palumbo, G.D. Prestwich, Disulfide-crosslinked hyaluronan-gelatin hydrogel films: a covalent mimic of the extracellular matrix for in vitro cell growth, Biomaterials 24 (21) (2003) 3825–3834.
[25] G.C. Yu, L.G. Wang, Y.Y. Han, Q.Y. He, clusterProfiler: an R Package for comparing biological themes among gene clusters, OMICS 16 (5) (2012) 284–287.
[26] D. Szklarczyk, A.L. Gable, K.C. Nastou, D. Lyon, R. Kirsch, S. Pyysalo, N. T. Doncheva, M. Legeay, T. Fang, P. Bork, L.J. Jensen, C. von Mering, The STRING database in 2021: customizable protein-protein networks, and functional characterization of user-uploaded gene/measurement sets (vol 49, pg D605, 2021), Nucleic Acids Res. 49 (18) (2021) 10800.
[27] P. Shannon, A. Markiel, O. Ozier, N.S. Baliga, J.T. Wang, D. Ramage, N. Amin, B. Schwikowski, T. Ideker, Cytoscape: a software environment for integrated models of biomolecular interaction networks, Genome Res. 13 (11) (2003) 2498–2504.
[28] G.D. Bader, C.W. Hogue, An automated method for finding molecular complexes in large protein interaction networks, BMC Bioinf. 4 (2003) 2.
[29] C. Wong, T.L. Wellman, K.M. Lounsbury, VEGF and HIF-1α expression are increased in advanced stages of epithelial ovarian cancer, Gynecol. Oncol. 91 (3) (2003) 513–517.
[30] S.Y. Oh, H.C. Kwon, S.H. Kim, J.S. Jang, M.C. Kim, K.H. Kim, J.Y. Han, C.O. Kim, S. J. Kim, J.S. Jeong, H.J. Kim, Clinicopathologic significance of HIF-1α, p53, and VEGF expression and preoperative serum VEGF level in gastric cancer, BMC Cancer 8 (2008) 123.
[31] K.L. Talks, H. Turley, K.C. Gatter, P.H. Maxwell, C.W. Pugh, P.J. Ratcliffe, A. L. Harris, The expression and distribution of the hypoxia-inducible factors HIF-1α and HIF-2α in normal human tissues, cancers, and tumor-associated macrophages, Am. J. Pathol. 157 (2) (2000) 411–421.
[32] K. Wang, M. Zhang, J. Wang, P. Sun, J.Z. Luo, H.Z. Jin, R. Li, C.Q. Pan, L.M. Lu, A systematic analysis identifies key regulators involved in cell proliferation and potential drugs for the treatment of human lung adenocarcinoma, Front. Oncol. 11 (2021) 737152.
[33] H.Y. Wang, L. Ye, Z. Xing, H.Q. Li, T.F. Lv, H.B. Liu, F. Zhang, Y. Song, CDCA7 promotes lung adenocarcinoma proliferation via regulating the cell cycle, Pathol. Res. Pract. 215 (11) (2019) 152559.
[34] C.H.Y. Cheung, C.L. Hsu, K.P. Chen, S.T. Chong, C.H. Wu, H.C. Huang, H.F. Juan, MCM2-regulated functional networks in lung cancer by multi-dimensional proteomic approach, Sci Rep-Uk 7 (2017) 13302.
[35] A. Urciuolo, G.G. Giobbe, Y. Dong, F. Michielin, L. Brandolino, M. Magnussen, O. Gagliano, G. Selmin, V. Scattolini, P. Raffa, P. Caccin, S. Shibuya, D. Scaglioni, X. Wang, J. Qu, M. Nikolic, M. Montagner, G.L. Galea, H. Clevers, M. Giomo, P. De Coppi, N. Elvassore, Hydrogel-in-hydrogel live bioprinting for guidance and control of organoids and organotypic cultures, Nat. Commun. 14 (1) (2023) 3128.
[36] Shuyi Qian, Yixiao Dong, Ju Qu, Xuechun Wang, Wang Zhang, Jia Chen, Fan Xu, Meihua Cui, Monica Giomo, Chenhan Liao, Manli Hu, Juan Xu, Ganlu Hu, Jie Zheng, Xianmin Zhu, Anna Urciuolo, Guoping Fan, and Nicola Elvassore. "Tunable Hydrogel Confinement via On-Chip 3D Printing for Studying Cancer Cell Migration". ACS Materials Letters 2023 5 (12), 3290-3298DOI: 10.1021/acsmaterialslett.3c00853.
[37] I. Acerbi, L. Cassereau, I. Dean, Q. Shi, A. Au, C. Park, Y.Y. Chen, J. Liphardt, E. S. Hwang, V.M. Weaver, Human breast cancer invasion and aggression correlates with ECM stiffening and immune cell infiltration, Integr Biol-Uk 7 (10) (2015) 1120–1134.
[38] F. Bordeleau, B.N. Mason, E.M. Lollis, M. Mazzola, M.R. Zanotelli, S. Somasegar, J. P. Califano, C. Montague, D.J. LaValley, J. Huynh, N. Mencia-Trinchant, Y.L. N. Abril, D.C. Hassane, L.J. Bonassar, J.T. Butcher, R.S. Weiss, C.A. Reinhart-King, Matrix stiffening promotes a tumor vasculature phenotype, P Natl Acad Sci USA 114 (3) (2017) 492–497.
[39] C.C. Wang, J.T. Yang, Mechanical forces: the missing link between idiopathic pulmonary fibrosis and lung cancer, Eur. J. Cell Biol. 101 (3) (2022) 151234.
[40] H. Sung, J. Ferlay, R.L. Siegel, M. Laversanne, I. Soerjomataram, A. Jemal, F. Bray, Global cancer statistics 2020: GLOBOCAN estimates of incidence and mortality worldwide for 36 cancers in 185 countries, Ca - Cancer J. Clin. 71 (3) (2021) 209–249.
[41] A. Miyazawa, S. Ito, S. Asano, I. Tanaka, M. Sato, M. Kondo, Y. Hasegawa, Regulation of PD-L1 expression by matrix stiffness in lung cancer cells, Biochem Bioph Res Co 495 (3) (2018) 2344–2349.
[42] S. Torrino, E.M. Grasset, S. Audebert, I. Belhadj, C. Lacoux, M. Haynes, S. Pisano, S. Abélanet, F. Brau, S.Y. Chan, B. Mari, W.M. Oldham, A.J. Ewald, T. Bertero, Mechano-induced cell metabolism promotes microtubule glutamylation to force metastasis, Cell Metab. 33 (7) (2021) 1342–1357.

[43] E.P. Mihalko, A.C. Brown, Material strategies for modulating epithelial to mesenchymal transitions, ACS Biomater. Sci. Eng. 4 (4) (2018) 1149–1161.
[44] S. Seetharaman, S. Etienne-Manneville, Cytoskeletal crosstalk in cell migration, Trends Cell Biol. 30 (9) (2020) 720–735.
[45] R. Fontana, A. Mestre-Farrera, J. Yang, Update on epithelial-mesenchymal plasticity in cancer progression, Annu. Rev. Pathol. 19 (2024) 133–156.
[46] M.C. Markowski, A.C. Brown, T.H. Barker, Directing epithelial to mesenchymal transition through engineered microenvironments displaying orthogonal adhesive and mechanical cues, J. Biomed. Mater. Res. A 100 (8) (2012) 2119–2127.
[47] D. Kim, E. You, J. Jeong, P. Ko, J.W. Kim, S. Rhee, DDR2 controls the epithelial-mesenchymal-transition-related gene expression via c-Myb acetylation upon matrix stiffening, Sci. Rep. 7 (1) (2017) 6847.
[48] V.C. Shukla, N. Higuita-Castro, P. Nana-Sinkam, S.N. Ghadiali, Substrate stiffness modulates lung cancer cell migration but not epithelial to mesenchymal transition, J. Biomed. Mater. Res. A 104 (5) (2016) 1182–1193.
[49] X. Xu, L. Ma, Y. Wu, L. Tang, Micropillar-based culture platform induces epithelial-mesenchymal transition in the alveolar epithelial cell line, J. Biomed. Mater. Res. A 106 (12) (2018) 3165–3174.
[50] C.D. Paul, P. Mistriotis, K. Konstantopoulos, Cancer cell motility: lessons from migration in confined spaces, Nat. Rev. Cancer 17 (2) (2017) 131–140.
[51] T. Stylianopoulos, J.D. Martin, V.P. Chauhan, S.R. Jain, B. Diop-Frimpong, N. Bardeesy, B.L. Smith, C.R. Ferrone, F.J. Hornicek, Y. Boucher, L.L. Munn, R. K. Jain, Causes, consequences, and remedies for growth-induced solid stress in murine and human tumors, Proc. Natl. Acad. Sci. U. S. A. 109 (38) (2012) 15101–15108.
[52] G.S. Karagiannis, T. Poutahidis, S.E. Erdman, R. Kirsch, R.H. Riddell, E. P. Diamandis, Cancer-associated fibroblasts drive the progression of metastasis through both paracrine and mechanical pressure on cancer tissue, Mol. Cancer Res. 10 (11) (2012) 1403–1418.
[53] Q. Chen, D. Yang, H. Zong, L. Zhu, L. Wang, X. Wang, X. Zhu, X. Song, J. Wang, Growth-induced stress enhances epithelial-mesenchymal transition induced by IL-6 in clear cell renal cell carcinoma via the Akt/GSK-3beta/beta-catenin signaling pathway, Oncogenesis 6 (8) (2017) e375.
[54] J. Barbazan, C. Perez-Gonzalez, M. Gomez-Gonzalez, M. Dedenon, S. Richon, E. Latorre, M. Serra, P. Mariani, S. Descroix, P. Sens, X. Trepat, D.M. Vignjevic, Cancer-associated fibroblasts actively compress cancer cells and modulate mechanotransduction, Nat. Commun. 14 (1) (2023) 6966.
[55] F. Bertillot, L. Andrique, C. Urena Martin, O. Zajac, L. de Plater, M.M. Norton, A. Richard, K. Alessandri, B.G. Gurchenkov, F. Fage, A. Asnacios, C. Lamaze, M. Das, J.L. Maitre, P. Nassoy, D. Matic Vignjevic, Compressive stress triggers fibroblasts spreading over cancer cells to generate carcinoma in situ organization, Commun. Biol. 7 (1) (2024) 184.
[56] J.M. Tse, G. Cheng, J.A. Tyrrell, S.A. Wilcox-Adelman, Y. Boucher, R.K. Jain, L. L. Munn, Mechanical compression drives cancer cells toward invasive phenotype, Proc. Natl. Acad. Sci. U. S. A. 109 (3) (2012) 911–916.
[57] Q. Chen, X.W. Zhou, A.J. Zhang, K. He, ACTN1 supports tumor growth by inhibiting Hippo signaling in hepatocellular carcinoma, J. Exp. Clin. Cancer Res. 40 (1) (2021) 23.
[58] P. Lappalainen, T. Kotila, A. Jégou, G. Romet-Lemonne, Biochemical and mechanical regulation of actin dynamics, Nat. Rev. Mol. Cell Biol. 23 (12) (2022) 836–852.
[59] M. Dogterom, G.H. Koenderink, Actin-microtubule crosstalk in cell biology, Nat. Rev. Mol. Cell Biol. 20 (1) (2019) 38–54.
[60] R. Ji, X.J. Zhu, Z.R. Wang, L.Q. Huang, Cortactin in epithelial-mesenchymal transition, Front. Cell Dev. Biol. 8 (2020) 585619.
[61] H.N. Meng, J.Y. Wu, Q. Huang, X. Yang, K.N. Yang, Y.X. Qiu, J.W. Ren, R.W. Shen, H. Qi, NEDD9 promotes invasion and migration of colorectal cancer cell line HCT116 via JNK/EMT, Oncol. Lett. 18 (4) (2019) 4022–4029.
[62] K. Stengel, Y. Zheng, Cdc42 in oncogenic transformation, invasion, and tumorigenesis, Cell. Signal. 23 (9) (2011) 1415–1423.
[63] Y.W. Liu, H.M. Hu, K.Y. Wang, C.B. Zhang, Y.Y. Wang, K. Yao, P. Yang, L. Han, C. S. Kang, W. Zhang, T. Jiang, Multidimensional analysis of gene expression reveals TGFB1I1-induced EMT contributes to malignant progression of astrocytomas, Oncotarget 5 (24) (2014) 12593–12606.
[64] D.A. Tumbarello, C.E. Turner, Hic-5 contributes to epithelial-mesenchymal transformation through a RhoA/ROCK-dependent pathway, J. Cell. Physiol. 211 (3) (2007) 736–747.
[65] P.S. Pardo, M.A. Lopez, A.M. Boriek, FOXO transcription factors are mechanosensitive and their regulation is altered with aging in the respiratory pump, Am J Physiol-Cell Ph 294 (4) (2008) C1056–C1066.
[66] Y.Y. Ma, H. Wang, PI3K/Akt/FoxO: a novel participant in signal transduction in bone cells under mechanical stimulation, Cell Biol. Int. 36 (10) (2012) 923–926.
[67] A.C. de Brachène, J.B. Demoulin, FOXO transcription factors in cancer development and therapy, Cell. Mol. Life Sci. 73 (6) (2016) 1159–1172.
[68] A. Desmaison, C. Frongia, K. Grenier, B. Ducommun, V. Lobjois, Mechanical stress impairs mitosis progression in multi-cellular tumor spheroids, PLoS One 8 (12) (2013) e80447.
[69] R.A. Moriarty, K.M. Stroka, Physical confinement alters sarcoma cell cycle progression and division, Cell Cycle 17 (19–20) (2018) 2360–2373.
[70] S. Nam, V.K. Gupta, H.P. Lee, J.Y. Lee, K.M. Wisdom, S. Varma, E.M. Flaum, C. Davis, R.B. West, O. Chaudhuri, Cell cycle progression in confining microenvironments is regulated by a growth-responsive TRPV4-PI3K/Akt-p27 signaling axis, Sci. Adv. 5 (8) (2019) eaaw6171.